

Theory of electron-plasmon coupling in semiconductors

Fabio Caruso and Feliciano Giustino

Department of Materials, University of Oxford, Parks Road, Oxford, OX1 3PH

(Dated: September 12, 2016)

The ability to manipulate plasmons is driving new developments in electronics, optics, sensing, energy, and medicine. Despite the massive momentum of experimental research in this direction, a predictive quantum-mechanical framework for describing electron-plasmon interactions in real materials is still missing. Here, starting from a many-body Green's function approach, we develop an *ab initio* approach for investigating electron-plasmon coupling in solids. As a first demonstration of this methodology, we show that electron-plasmon scattering is the primary mechanism for the cooling of hot carriers in doped silicon, it is key to explain measured electron mobilities at high doping, and it leads to a quantum zero-point renormalization of the band gap in agreement with experiment.

Plasmons are collective oscillations of electrons in solids that can exist even in the absence of an external driving field. During the last decade plasmons generated tremendous interest owing to the rise of plasmonics, the science of manipulating light and light-matter interactions using surface plasmon polaritons¹. Plasmonic materials and devices show exceptional promise in the areas of nanoelectronics², photovoltaics^{3,4}, and radiation treatment therapy^{5,6}. While the electrodynamic laws governing plasmonics at macroscopic length-scales are well understood^{7,8}, little is known about the interaction of plasmons with matter at the atomic scale. For example questions pertaining the interaction between plasmons and charge carriers in semiconductors have not been addressed on quantitative grounds, yet they are critical to engineering materials for semiconductor plasmonics⁹. Up to now microscopic quantum-mechanical theories of electron-plasmon interactions have been limited to idealised models of solids, such as the homogeneous electron gas^{10,11}. While these models laid the theoretical foundations of the theory, they are not suitable for predictive calculations.

In this work we introduce a first-principles method to study electron-plasmon coupling in solids. As a first application we focus on doped semiconductors, where the manifestations of electron-plasmon coupling are most spectacular. In contrast to metals and insulators, doped semiconductors can sustain ‘thermal plasmons’, that is plasmons with energies comparable to those of lattice vibrations. Under these conditions electron-plasmon interactions can modify carrier lifetimes, mobilities, and optical gaps in a manner similar to electron-phonon interactions. Using this method we find that, in the case of degenerate *n*-type silicon, thermal plasmons lead to ultrafast relaxation of hot carriers, provide the main bottleneck to carrier mobility, and induce a zero-point renormalization of the band gap that exceeds the phonon-induced renormalization.

In free-electron metals the energy of a plasmon is $\hbar\omega_P = (\hbar^2 e^2 n / \epsilon_0 m_e)^{1/2}$, where \hbar is the Planck constant, ϵ_0 is the dielectric permittivity of vacuum, and e , m_e , and n are the electron charge, mass, and density, respectively. At typical metallic densities, as in common plasmonic

metals such as Au and Ag ($n = 3\text{--}8 \cdot 10^{22} \text{ cm}^{-3}$), plasmons have characteristic energies in the range of 5-10 eV. In these cases electron-plasmon scattering is suppressed by the energy-conservation selection rule. At variance with this scenario, in doped semiconductors the electron mass in the above expression is replaced by the band effective mass, and the vacuum permittivity is replaced by the dielectric constant. As a result the plasmon energy is considerably smaller, and at standard doping levels it can easily reach the thermal range, $\hbar\omega_P = 10\text{--}100 \text{ meV}$. Under these conditions electrons can exchange energy with plasmons, hence the populations of carriers and plasmons become mutually coupled.

In order to investigate the consequences of this coupling, we start by characterizing plasmonic excitations in doped silicon from first principles. Figure 1 shows the calculated electron energy loss function, $\text{Im } \epsilon^{-1}(\mathbf{q}, \omega)$, which encodes information about how an electron travelling through a solid dissipates energy¹². Here $\epsilon^{-1}(\mathbf{q}, \omega)$ denotes the head of the inverse dielectric matrix for the wavevector \mathbf{q} and the frequency ω , evaluated within the random phase approximation^{13,14}. In the case of intrinsic silicon at zero temperature (Fig. 1a) the loss function exhibits a continuous energy distribution (brown region) with a threshold set by the fundamental gap. This broad structure arises from interband transitions from the filled valence bands to the empty conduction bands, and physically corresponds to the generation of electron-hole pairs by impact ionization. This is schematically indicated as ‘process 1’ in Fig. 1d. The scenario changes drastically in the case of doped silicon. Fig. 1b and Fig. 1c show the loss function of heavily *n*-doped silicon, corresponding to $n = 2.5 \cdot 10^{19} \text{ cm}^{-3}$ and $n = 2.5 \cdot 10^{20} \text{ cm}^{-3}$, respectively. As a result of the partial filling of the conduction band valley near the *X* point of the Brillouin zone, new dissipation channels become available. In particular, ‘process 2’ in Fig. 1b corresponds to the generation of low-energy electron-hole pairs. In this case we see sharp structures which define ‘ghost’ bands as a function of the momentum loss $\hbar\mathbf{q}$. These features are understood in terms of intraband and interband transitions from occupied initial states with wavevector \mathbf{k} near the bottom of the conduction band to empty final states of wavevec-

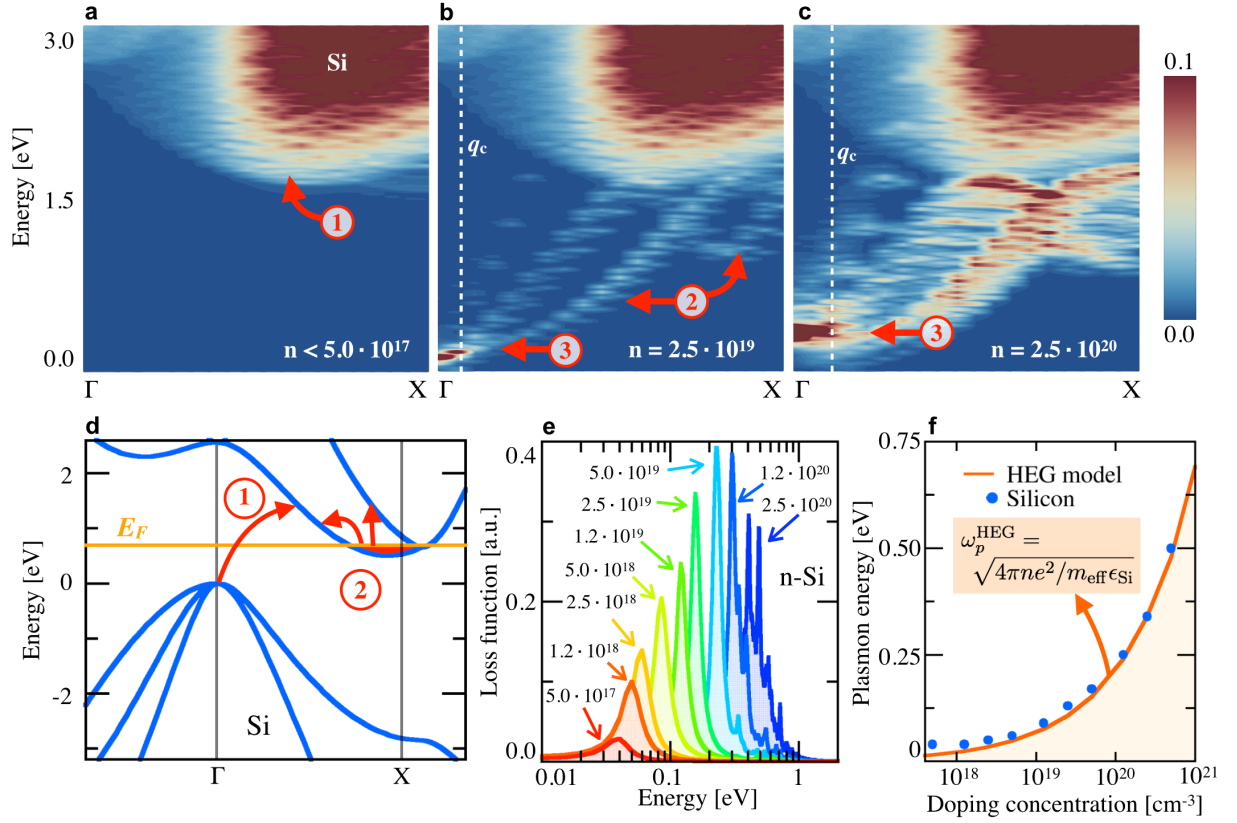


Figure 1. (a–c) Calculated electron-energy loss function of n -type silicon for momentum transfers \mathbf{q} along the Γ X high-symmetry line. The carrier density increases from left to right, from 10^{17} to 10^{20} cm^{-3} . (d) LDA band structure of silicon, and Fermi level (E_F) for $n = 2.5 \cdot 10^{20}$ cm^{-3} . The step-like structures in (b) and (c) are only a numerical artifact arising from the limited Brillouin-zone sampling. (e) Variation of the plasmon peak in the loss function vs. carrier density, evaluated at $\mathbf{q} = 0$. (f) Plasma energies extracted from peaks in (e), plotted vs. carrier concentration (blue dots). The red line corresponds to the analytical result obtained for a homogeneous electron gas with the calculated isotropic effective mass and dielectric constant of silicon ($m_{\text{eff}} = 0.25$, $\epsilon_{\text{Si}} = 12$).

tor $\mathbf{k} + \mathbf{q}$. The intensity of these features increases with the doping level from Fig. 1b to Fig. 1c. The peaks in the loss function denoted by ‘process 3’ cannot be explained in terms of the previous two mechanisms. In fact for $\mathbf{q} = 0$ these structures are much sharper than those described above, and exist below the energy (momentum) threshold for the generation of electron-hole pairs via interband (intraband) transitions. These processes correspond to the emission of plasmons, and are characterised by well-defined energy resonances, as it is shown by Fig. 1e for $\mathbf{q} = 0$. By mapping these plasmon peaks in the loss function we can see in Fig. 1f that the plasmon energy $\hbar\omega_P$ scales with the carrier concentration, following the same trend expected for a homogeneous electron gas. In this figure we also see that the plasmon energy is highly tunable via doping, from thermal energies at carrier densities around 10^{18} cm^{-3} , to half an electronvolt at densities near 10^{21} cm^{-3} .

At large momentum transfer $\hbar\mathbf{q}$ the distinction between plasmons and electron-hole pairs is no longer meaningful, since the fluctuations of the charge density

happen on length-scales approaching the size of the crystal unit cell. In the following we identify plasmons in the loss function by analogy with the homogeneous electron gas, where well-defined plasma excitations exist only for momenta below the electron-hole continuum¹⁵. For a plasmon of energy $\hbar\omega_P$ the critical momentum is given by the wavevector $q_c = k_F [(1 + \hbar\omega_P/\epsilon_F)^{1/2} - 1]$, with k_F and ϵ_F being the Fermi wavevector and the Fermi energy, respectively. The critical wavevector q_c marks the onset of Landau damping, that is, the decay of a plasmon upon excitation of an electron-hole pair. Thus, for $q < q_c$ thermal plasmons are undamped collective phenomena with lifetimes set by plasmon-phonon and plasmon-plasmon scattering processes¹⁶. This boundary is shown as white dashed lines in Fig. 1b and Fig. 1c.

In order to investigate the effects of plasmons on the electronic structure we generalise Pines’ theory of electron-plasmon interactions in the homogeneous electron gas¹⁵ to *ab initio* calculations for crystalline solids. Our strategy consists of the following steps: (i) We identify the energy vs. wavevector dispersion relations of

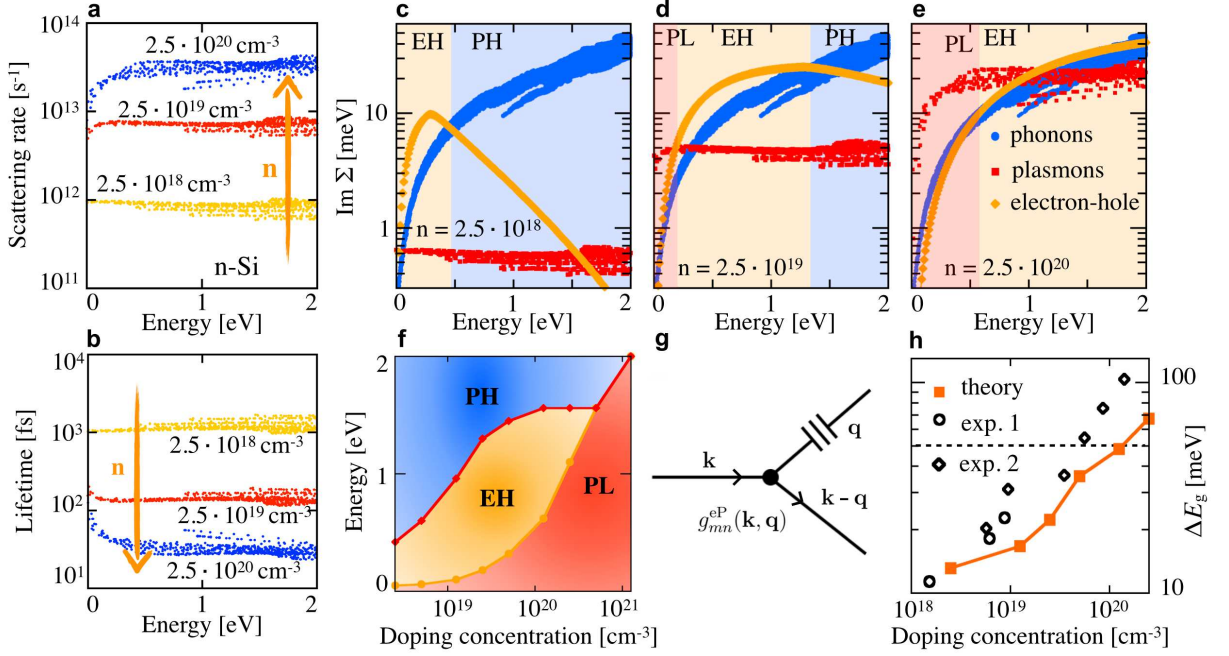


Figure 2. (a) Calculated rates of electron scattering by plasmons, and (b) corresponding electron lifetimes in doped silicon, for several carrier concentrations. The electron energy is referred to the conduction band edge. (c–e) Comparison between the imaginary part of the electron-plasmon self-energy, the electron-phonon self-energy, and the self-energy associated with electron-hole pair generation. The carrier concentration increases from (c) to (e), and the electron energy is referred to the conduction band edge. Shaded regions indicate the dominant scattering mechanism at a given electron energy, and ‘PL’, ‘PH’, ‘EH’ stand for plasmons, phonons, and electron-hole pairs, respectively. (f) Energy vs. doping map of the largest contribution to the electron self-energy. The energy is referred to the conduction band edge. (g) Diagrammatic representation of the electron plasmon scattering process. (h) Calculated plasmon-induced band gap renormalization in silicon as a function of carrier density (orange squares and line), compared to the optical data from Ref.¹⁷ (experiment 1) and Ref.¹⁸ (experiment 2). The dashed horizontal line indicates the renormalization of the band gap by electron-phonon interactions, as reported by Ref.¹⁹.

thermal plasmons. This is achieved by determining the plasma energies from the poles of $\text{Im} \epsilon^{-1}(\mathbf{q}, \omega)$ for momenta below the critical wavevector q_c ²⁰. (ii) We single out the plasmonic contribution to the macroscopic dielectric function ϵ_M via the Taylor expansion $\epsilon_P(\mathbf{q} + \mathbf{G}, \omega) =$

$\frac{\partial \epsilon_M}{\partial \omega} \Big|_{\omega=\omega_P(\mathbf{q})} [\omega - \omega_P(\mathbf{q})] + i\eta$ in the vicinity of the plasmon frequency $\omega_P(\mathbf{q})$. (iii) We calculate the electron-plasmon self-energy starting from many-body perturbation theory, and retain only the plasmonic screening. This leads to the retarded electron self-energy in Raleigh-Schrödinger perturbation theory²¹:

$$\Sigma_{n\mathbf{k}}^{\text{eP}} = \int \frac{d\mathbf{q}}{\Omega_{\text{BZ}}} \sum_m |g_{mn}^{\text{eP}}(\mathbf{k}, \mathbf{q})|^2 \left[\frac{n_{\mathbf{q}} + f_{m\mathbf{k}+\mathbf{q}}}{\varepsilon_{n\mathbf{k}} - \varepsilon_{m\mathbf{k}+\mathbf{q}} + \hbar\omega_P(\mathbf{q}) + i\eta} + \frac{n_{\mathbf{q}} + 1 - f_{m\mathbf{k}+\mathbf{q}}}{\varepsilon_{n\mathbf{k}} - \varepsilon_{m\mathbf{k}+\mathbf{q}} - \hbar\omega_P(\mathbf{q}) + i\eta} \right]. \quad (1)$$

In this expression \mathbf{k} and \mathbf{q} are Bloch wavevectors, m and n band indices, $\varepsilon_{n\mathbf{k}}$ and $\varepsilon_{m\mathbf{k}+\mathbf{q}}$ Kohn-Sham eigenvalues, $n_{\mathbf{q}}$ and $f_{m\mathbf{k}+\mathbf{q}}$ Bose-Einstein and Fermi-Dirac occupations, respectively, and η a positive infinitesimal. The summation runs over all states and the integral is over the Brillouin zone of volume Ω_{BZ} . The quantities $g_{mn}^{\text{eP}}(\mathbf{k}, \mathbf{q})$ represent the electron-plasmon scattering matrix elements between the initial state $\psi_{n\mathbf{k}}$ and the final

state $\psi_{m\mathbf{k}+\mathbf{q}}$, and are given by:

$$g_{mn}^{\text{eP}}(\mathbf{k}, \mathbf{q}) = \left[\frac{\varepsilon_0 \Omega}{e^2 \hbar} \frac{\partial \epsilon(\mathbf{q}, \omega)}{\partial \omega} \right]_{\omega_P(\mathbf{q})}^{-\frac{1}{2}} \frac{1}{|\mathbf{q}|} \langle \psi_{m\mathbf{k}+\mathbf{q}} | e^{i\mathbf{q} \cdot \mathbf{r}} | \psi_{n\mathbf{k}} \rangle, \quad (2)$$

with Ω being the volume of one unit cell. Eqs. (1) and (2) are derived in the Appendix. The present approach to electron-plasmon coupling in semiconductors is formally identical to the standard theory of electron-

phonon interactions²². In particular, the $1/|\mathbf{q}|$ divergence of the electron-plasmon matrix elements at long wavelengths is reminiscent of the Fröhlich interaction between electrons and longitudinal-optical phonons in polar semiconductors^{23,24}. This analogy is consistent with the fact that bulk plasmons are longitudinal waves. We now analyse the consequences of the self-energy in Eq. (1).

From the imaginary part of the self-energy in Eq. (1) we obtain the rate of electron scattering by thermal plasmons, using $\Gamma_{n\mathbf{k}} = 2\text{Im}\Sigma_{n\mathbf{k}}/\hbar$. Physically the two denominators in Eq. (1) describe processes of one-plasmon absorption and emission, respectively. A diagrammatic representation of these processes is given in Fig. 2g. Multi-plasmon processes are not included in the present formalism, similarly to the case of electron-phonon interactions²², therefore we limit our discussion to low temperatures ($n_{\mathbf{q}} \ll 1$). Fig. 2a shows the calculated electron-plasmon scattering rates in *n*-type silicon. The carrier energies are referred to the conduction band edge. For standard doping levels ($n < 10^{18} \text{ cm}^{-3}$) the scattering rates fall below 10^{11} s^{-1} as a result of the low intensity of the plasmon peaks in Fig. 1e, which is reflected in the strength of the matrix elements in Eq. (2). However, at doping levels above 10^{18} cm^{-3} , the strength of the plasmon peak in the loss function increases considerably, and the frequency of scattering by thermal plasmons becomes comparable to electron-phonon scattering rates, 10^{12} - 10^{14} s^{-1} ^{25,26}. Fig. 2a shows that at even higher doping levels these rates keep increasing by orders of magnitude, and eventually dominate the cooling dynamics of excited carriers.

A complementary perspective on the carrier dynamics is provided by Fig. 2b. Here we show the electron lifetimes corresponding to the rates in Fig. 2a, calculated as $\tau_{n\mathbf{k}} = 1/\Gamma_{n\mathbf{k}}$. Time-resolved reflectivity measurements of non-degenerate silicon ($n = 10^{17} \text{ cm}^{-3}$ electrons photo-excited at $\sim 0.8 \text{ eV}$ above the band edge) indicate thermalisation rates around 350 fs ²⁷. In the same doping range our calculations yield plasmon-limited carrier lifetimes well above 10 ps , indicating that under these conditions electron-plasmon scattering is ineffective. However, the scenario changes drastically for degenerate silicon, for which we calculate lifetimes in the sub-picosecond regime. In particular, for doping levels in the range 10^{19} - 10^{20} cm^{-3} the electron-plasmon scattering reduces the carrier lifetimes to 25 - 150 fs . In these conditions electron-phonon and electron-plasmon scattering become competing mechanisms for hot-carrier thermalisation.

In order to quantify the importance of electron-plasmon scattering we compare in Fig. 2c-e the imaginary part of the electron self-energy associated with (i) electron-plasmon interactions, (ii) electron-phonon interactions, and (iii) and electron-hole pair generation. The methods of calculation of (ii) and (iii) are described in the Supplemental Materials¹⁶. From this comparison we deduce that plasmons become increasingly important towards higher doping, and their effect is most pronounced in the vicinity of the band edge. By identifying the

largest contribution for each doping level and for each electron energy, we can construct the ‘scattering phase diagram’ shown in Fig. 2f. This diagram illustrates the regions in the energy vs. doping space where each scattering mechanism dominates. Unexpectedly in degenerate silicon electron-plasmon scattering represents the dominant mechanism for hot-carrier relaxation. This finding could provide new opportunities in the study of semiconductor-based plasmonics, for example by engineering the doping concentration so as to selectively target the ‘plasmon region’ in Fig. 2f.

We also evaluated the impact of electron-plasmon scattering processes on the carrier mobility in silicon, by using the lifetimes computed above as a first approximation to the carrier relaxation times. As shown in Fig. S1¹⁶, the explicit inclusion of electron-phonon scattering is essential to achieve a good agreement with experiment. On the other hand, were we to consider only electron-phonon scattering and electron-hole pair generation, we would overestimate the experimental mobilities by more than an order of magnitude.

The real part of the electron self-energy in Eq. (1) allows us to evaluate the renormalization of the electron energy levels arising from the dressing of electron quasiparticles by virtual plasmons. Since the renormalization of semiconductor band gaps induced by electron-phonon interactions attracted considerable interest lately²⁸⁻³³, we here concentrate on the quantum zero-point renormalization of the fundamental gap of silicon. Computational details of the calculations and convergence tests are reported in the Supplemental Material¹⁶. Considering for definiteness a carrier density of $n = 2.5 \cdot 10^{20} \text{ cm}^{-3}$, we find that the electron-plasmon coupling lowers the conduction band edge by $\Delta E_c = -37 \text{ meV}$ at zero temperature, and rises the valence band edge by $\Delta E_v = 30 \text{ meV}$. For carrier concentrations of $2.5 \cdot 10^{19} \text{ cm}^{-3}$ and $2.5 \cdot 10^{20} \text{ cm}^{-3}$ we verified that the BGN changes by less than 1 meV for temperatures up to 600 K (see Supplemental Material¹⁶). As a result at this doping concentration the band gap redshifts by $\Delta E_g = \Delta E_c - \Delta E_v = -67 \text{ meV}$. This phenomenology is entirely analogous to the zero-point renormalization from electron-phonon interactions²⁹. Our finding is consistent with the fact that the self-energy in Eq. (1) and the matrix element in Eq. (2) are formally identical to those that one encounters in the study of the Fröhlich interaction. The doping-induced band gap renormalization was also reported in a recent work on monolayer MoS_2 ³⁴, therefore we expect this feature to hold general validity in doped semiconductors. In order to perform a quantitative comparison with experiment, we show in Fig. 2h our calculated plasmonic band gap renormalization and measurements of the indirect absorption onset in doped silicon^{17,18}. We can see that there is already good agreement between theory and experiment, even if we are considering only electron-plasmon couplings as the sole source of band gap renormalization. Surprisingly the magnitude of the renormalization, 15 - 70 meV , is compa-

rable to the zero-point shift induced by electron-phonon interactions, 60-72 meV¹⁹.

In summary, we presented an *ab initio* approach to electron-plasmon coupling in doped semiconductors. We showed that electron-plasmon interactions are strong and ubiquitous in a prototypical semiconductor such as doped silicon, as revealed by their effect on carrier dynamics, transport, and optical properties. This finding calls for a systematic investigation of electron-plasmon couplings in a wide class of materials. More generally, a detailed understanding of the interaction between electrons and thermal plasmons via predictive atomic-scale calculations could provide a key into the design of plasmonic semiconductors, for example by using phase diagrams such as in Fig. 2f to tailor doping levels and excitation energies to selectively target strong-coupling regimes. Finally, the striking similarity between electron-plasmon coupling and the Fröhlich coupling in polar materials may open new avenues to probe plasmon-induced photoemission kinks³⁵, polaron satellites^{36–38}, as well as superconductivity, in analogy with the case of electron-phonon interactions.^{39–44}.

ACKNOWLEDGMENTS

F.C. acknowledges discussions with C. Verdi and S. Poncé. The research leading to these results has received funding from the Leverhulme Trust (Grant RL-2012-001), the Graphene Flagship (EU FP7 grant no. 604391), the UK Engineering and Physical Sciences Research Council (Grant No. EP/J009857/1). Supercomputing time was provided by the University of Oxford Advanced Research Computing facility (<http://dx.doi.org/10.5281/zenodo.22558>) and the ARCHER UK National Supercomputing Service.

Appendix A: Electron self-energy for the electron-plasmon interaction

Here we provide a derivation of the electron-plasmon coupling strength and the self-energy [Eq. (1) and (2)] by generalizing the theory of electron-plasmon interaction for the homogeneous electron gas to the case of crystalline solids. We start from the electron self-energy in the *GW* approximation^{45–47}:

$$\Sigma_{n\mathbf{k}}(\omega) = \frac{i\hbar}{2\pi} \sum_{m\mathbf{G}\mathbf{G}'} \int \frac{d\mathbf{q}}{\Omega_{\text{BZ}}} M_{\mathbf{G}}^{mn}(\mathbf{k}, \mathbf{q})^* M_{\mathbf{G}'}^{mn}(\mathbf{k}, \mathbf{q}) \int d\omega' \frac{W_{\mathbf{G}\mathbf{G}'}(\mathbf{q}, \omega')}{\hbar\omega + \hbar\omega' + \mu - \tilde{\epsilon}_{m\mathbf{k}+\mathbf{q}}}, \quad (\text{A1})$$

where $M_{\mathbf{G}}^{mn}(\mathbf{k}, \mathbf{q}) = \langle \psi_{m\mathbf{k}+\mathbf{q}} | e^{i(\mathbf{q}+\mathbf{G})\cdot\mathbf{r}} | \psi_{n\mathbf{k}} \rangle$ are the optical matrix elements, μ is the chemical potential, and $\tilde{\epsilon}_{m\mathbf{k}+\mathbf{q}} = \epsilon_{m\mathbf{k}+\mathbf{q}} + i\eta \text{sign}(\mu - \epsilon_{m\mathbf{k}+\mathbf{q}})$. The matrix $W_{\mathbf{G}\mathbf{G}'}(\mathbf{q}, \omega') = v(\mathbf{q} + \mathbf{G}) \epsilon_{\mathbf{G}\mathbf{G}'}^{-1}(\mathbf{q}, \omega')$ represents the screened Coulomb interaction, and is obtained from the bare Coulomb interaction $v(\mathbf{q}) = e^2/\epsilon_0\Omega|\mathbf{q}|^2$ via the inverse dielectric matrix $\epsilon_{\mathbf{G}\mathbf{G}'}^{-1}(\mathbf{q}, \omega')$. The spectral representation of W is given by:

$$W_{\mathbf{G}\mathbf{G}'}(\mathbf{q}, \omega) = \frac{v(\mathbf{q} + \mathbf{G})}{\pi} \int_0^\infty d\omega' \frac{2\omega'}{\omega^2 - (\omega')^2} \text{Im} \epsilon_{\mathbf{G}\mathbf{G}'}^{-1}(\mathbf{q}, \omega'). \quad (\text{A2})$$

The dielectric matrix may be decomposed into:

$$\epsilon_{\mathbf{G}\mathbf{G}'}^{-1}(\mathbf{q}, \omega) = \epsilon_{\mathbf{M}}^{-1}(\mathbf{q} + \mathbf{G}, \omega) \delta_{\mathbf{G}\mathbf{G}'} + \epsilon_{\mathbf{G}\mathbf{G}'}^{-1}(\mathbf{q}, \omega) (1 - \delta_{\mathbf{G}\mathbf{G}'}). \quad (\text{A3})$$

where $\epsilon_{\mathbf{M}}^{-1}(\mathbf{q} + \mathbf{G}, \omega)$ is the inverse macroscopic dielectric function. Since the plasmon energy $\hbar\omega_{\text{P}}(\mathbf{q})$ is defined by the condition $\epsilon_{\mathbf{M}}(\mathbf{q} + \mathbf{G}, \omega_{\text{P}}(\mathbf{q})) = 0$, the plasmonic contribution to the dielectric matrix ϵ_{P} can be singled out by Taylor-expanding $\epsilon_{\mathbf{M}}$ around the plasmon energy. Following Pines and Schrieffer¹¹ we have:

$$\epsilon_{\text{P}}(\mathbf{q} + \mathbf{G}, \omega) = \left. \frac{\partial \epsilon_{\mathbf{M}}}{\partial \omega} \right|_{\omega=\omega_{\text{P}}(\mathbf{q})} [\omega - \omega_{\text{P}}(\mathbf{q})] + i\eta. \quad (\text{A4})$$

Making use of the identity $(a + i\eta)^{-1} = P(1/a) + i\pi\delta(a)$, and combining Eqs. (A1), (A2), and (A4) yields the electron-plasmon self-energy:

$$\Sigma_{n\mathbf{k}}^{\text{eP}}(\omega) = \frac{i\hbar}{2\pi} \sum_{m\mathbf{G}} \int \frac{d\mathbf{q}}{\Omega_{\text{BZ}}} |M_{\mathbf{G}}^{nm}(\mathbf{k}, \mathbf{q})|^2 \int d\omega' \frac{2\omega_{\text{P}}(\mathbf{q})}{\omega'^2 - [\omega_{\text{P}}(\mathbf{q})]^2} \left[\left. \frac{\partial \epsilon_{\mathbf{M}}}{\partial \omega} \right|_{\omega=\omega_{\text{P}}(\mathbf{q})} \right]^{-1} \frac{v(\mathbf{q} + \mathbf{G})}{\omega + \omega' + \mu - \tilde{\epsilon}_{m\mathbf{k}+\mathbf{q}}}. \quad (\text{A5})$$

This expression may be recast into the form of a self-energy describing the interaction between electrons and bosons in the Migdal approximation^{21,48–51}:

$$\Sigma_{n\mathbf{k}}^{\text{eP}}(\omega) = \frac{i\hbar}{2\pi} \sum_m \int \frac{d\mathbf{q}}{\Omega_{\text{BZ}}} \int d\omega' |g_{mn}^{\text{eP}}(\mathbf{k}, \mathbf{q})|^2 D_{\mathbf{q}}(\omega') G_{m\mathbf{k}+\mathbf{q}}(\omega + \omega'). \quad (\text{A6})$$

Since for doped semiconductors q_c is typically within the first Brillouin zone, we dropped the dependence on the

reciprocal lattice vectors \mathbf{G} . The matrix elements ap-

appearing in this expression are defined in Eq. (2); G represents the standard non-interacting (Kohn-Sham) electron Green's function, $G_{n\mathbf{k}}(\omega) = [\hbar\omega - (\varepsilon_{n\mathbf{k}} - \mu)]^{-1}$, and we introduced the 'plasmon propagator': $D_{\mathbf{q}}(\omega) = 2\omega_P(\mathbf{q})/[\hbar(\omega^2 - \omega_P^2(\mathbf{q}))]$. Equation (A6) represents the prototypical electron self-energy arising from electron-boson interactions. From this expression the result in Eq. (1) follows by standard integration in the complex plane²¹.

For completeness we note that Eq. (A6) can also be derived from the electron-boson coupling Hamiltonian $\hat{H}^{\text{eP}} = \Omega_{\text{BZ}}^{-2} \sum_{nm} \int d\mathbf{k} d\mathbf{q} g_{nm}^{\text{eP}}(\mathbf{k}, \mathbf{q}) \hat{c}_{m\mathbf{k}+\mathbf{q}}^\dagger \hat{c}_{n\mathbf{k}} (\hat{b}_{\mathbf{q}} + \hat{b}_{-\mathbf{q}}^\dagger)$, where $\hat{b}_{-\mathbf{q}}^\dagger$ ($\hat{b}_{\mathbf{q}}$) and $\hat{c}_{m\mathbf{k}+\mathbf{q}}^\dagger$ ($\hat{c}_{n\mathbf{k}}$) are the boson and fermion creation (destruction) operators, respectively. As a consistency check, we note that the electron-plasmon coupling coefficients Eq. (2) reduce to the results of Pines and Schrieffer for homogeneous systems¹¹. In particular, for an homogeneous electron gas we have $M_{\mathbf{G}}^{nm}(\mathbf{k}, \mathbf{q}) = \delta_{nm}$ and $\epsilon_M = 1 - \omega_P(\mathbf{q})/\omega^2$. In this case, the partial derivative in the definition of

the electron-plasmon coupling coefficients can be evaluated analytically, giving the results of Ref.¹¹, $g^{\text{eP}}(\mathbf{q}) = (2\pi e^2 \hbar \omega_P(\mathbf{q}) / \epsilon_0 q^2)^{\frac{1}{2}}$.

Finally, we emphasize that the structure of Eq. (A5) stems directly from the identification of the plasmonic contribution to the dielectric function through the linearization of Eq. (A4), and it is reflected in the inclusion of the plasmon oscillator strength $\frac{\partial \epsilon_M}{\partial \omega}|_{\omega=\omega_P(\mathbf{q})}$ in the coupling coefficients [Eq. (2)]. This procedure distinguishes the electron-plasmon self-energy from the conventional GW self-energy in the plasmon-pole approximation, and justifies its application to the study of thermal plasmons in doped semiconductors.

Appendix B: Plasmon damping

To investigate the effects of extrinsic carriers on thermal plasmons, we consider the Fermi golden rule for the rate of change of the plasmon distribution function¹¹:

$$R_{\mathbf{q}} = \frac{2\pi}{\hbar} \sum_{\mathbf{k}} \int \frac{d\mathbf{k}}{\Omega_{\text{BZ}}} \sum_{nm} |g_{nm}^{\text{eP}}(\mathbf{k}, \mathbf{q})|^2 [(n_{\mathbf{q}} + 1) f_{n\mathbf{k}+\mathbf{q}} (1 - f_{m\mathbf{k}}) - n_{\mathbf{q}} f_{m\mathbf{k}} (1 - f_{n\mathbf{k}+\mathbf{q}})] \delta(\epsilon_{m\mathbf{k}} + \hbar\omega_P(\mathbf{q}) - \epsilon_{n\mathbf{k}+\mathbf{q}}) \quad (\text{B1})$$

where $\hbar\omega_P(\mathbf{q})$ are plasmon energies, g^{eP} electron-plasmon coupling coefficients, and n/f are Bose/Fermi occupation factors for plasmons/electrons. In practice, the first term accounts for the increase of the plasmon population induced by the absorption of an electron-hole pair, whereas the inverse process is described by the second term. Thermal plasmons are well defined for momenta smaller than the critical momentum cutoff given by the wavevector: $q_c = k_F [(1 + \hbar\omega_P/\varepsilon_F)^{1/2} - 1]$, with k_F and ε_F being the Fermi wavevector and the Fermi energy, respectively. By definition (see, e.g.,¹⁵) q_c is the smallest momentum satisfying the condition $\hbar\omega_P(\mathbf{q}) = \epsilon_{n\mathbf{k}+\mathbf{q}} - \epsilon_{m\mathbf{k}}$. Thus for $q < q_c$, the Dirac δ in Eq. (B1) vanishes, indicating that, while excited carriers may decay upon plasmon emission, the inverse processes, whereby a thermal plasmon decays upon emission of an electron-hole pair, is forbidden. Therefore, thermal plasmons are *undamped* by other electronic processes, and their decay for $q < q_c$ may be ascribed exclusively to plasmon-phonon and plasmon-plasmon scattering.

To exemplify the effect of Landau damping on the plasmon dispersion, we illustrate in Fig. 3 the plasmon peak in the loss function of silicon at a doping concentration of $1.25 \cdot 10^{20} \text{ cm}^{-3}$. At these carrier concentration, we obtain a momentum cutoff $q_c = 0.05$ in units of $2\pi/a$, with a being the lattice constant. For $q < q_c$, the loss function exhibit well defined plasmon peak with a peak intensity larger than the continuum of electron-hole excitations. For $q > q_c$, on the other hand, the plasmon

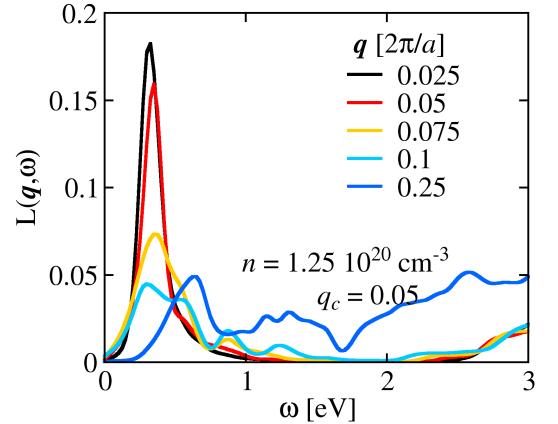


Figure 3. Momentum dependence of plasmon peak in the loss function of silicon at a doping concentration of $1.25 \cdot 10^{20} \text{ cm}^{-3}$, corresponding to a critical momentum cutoff $q_c = 0.05$ in $2\pi/a$ units.

intensity is reduced as a consequence of the lifetime effects introduced by Landau damping, and its intensity becomes essentially indistinguishable from the spectral signatures of electron-hole pairs.

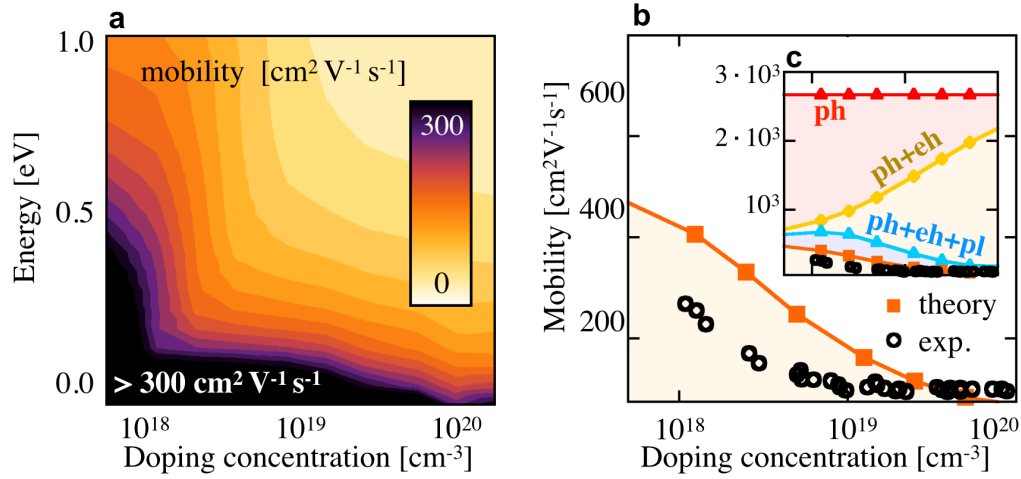


Figure 4. (a) Calculated electron mobility in n -type silicon, as a function of carrier density and energy relative to the chemical potential. (b) Comparison between calculated and measured electron mobilities in silicon as a function of doping. The black circles indicate experimental low-temperature mobility data from Ref.⁵². The orange squares and line represent our complete calculation including electron-plasmon (pl), electron-phonon (ph), electron-hole (eh), and impurity scattering. (c) Partial contributions to the mobility are shown as red (ph), and yellow (ph+eh).

Appendix C: Plasmon-limited mobility

We now evaluate the impact of electron-plasmon scattering processes on the carrier mobility in silicon. In the relaxation-time approximation the mobility is given by $\mu = e\tau^{\text{tot}}/m_e m^*$, where m^* is the conductivity effective mass, that is the harmonic average of the longitudinal and transverse masses, and τ^{tot} is the scattering time arising from processes involving plasmons (eP), phonons (ep), electron-hole pairs (eh), and impurities (i). Noting that scattering time and relaxation time differ by less than 10% at low carrier concentrations⁵³, we follow Matthiessen's rule to calculate $\tau_{n\mathbf{k}}^{\text{tot}} = \hbar/2 \text{Im}(\Sigma_{n\mathbf{k}}^{\text{ep}} + \Sigma_{n\mathbf{k}}^{\text{eP}} + \Sigma_{n\mathbf{k}}^{\text{eh}} + \Sigma_{n\mathbf{k}}^{\text{i}})$, where $\Sigma_{n\mathbf{k}}^{\text{ep}}$, $\Sigma_{n\mathbf{k}}^{\text{eh}}$, and $\Sigma_{n\mathbf{k}}^{\text{i}}$ are the electron self-energies associated with each interaction.

Strictly speaking the mobility μ is an average property of all the carriers in a semiconductor; however, for illustration purposes, it is useful to consider a 'single-electron' mobility obtained as $\mu_{n\mathbf{k}} = e\tau_{n\mathbf{k}}^{\text{tot}}/m_e m^*$. This quantity is shown in Fig. 4a. In this figure we see that the mobility decreases as one moves higher up in the conduction band; this behavior relates to the increased phase-space availability for electronic transitions. In addition we see that the mobility decreases with increasing carrier concentration. In order to analyse this trend we give a breakdown of the various sources of scattering

in Fig. 4c, and we compare our calculations to experiment. Here we show the carrier mobility at 300 K averaged on the Fermi surface defined by the doping level. Electrical measurements at high doping⁵² yield mobilities in the range of $100\text{--}300 \text{ cm}^2 \text{V}^{-1} \text{s}^{-1}$ for carrier densities between 10^{18} and 10^{20} cm^{-3} ; these data are shown as black circles in Fig. 4b-c. Were we to consider only electron-phonon scattering and electron-hole pair generation, we would overestimate the experimental mobilities by more than an order of magnitude (red and yellow lines in Fig. 4c). Impurity scattering reduces this discrepancy to some extent, but there remains a residual difference at the highest doping levels. It is only upon accounting for electron-plasmon scattering that the calculations exhibit a trend in qualitative and even semi-quantitative agreement with experiments throughout the entire doping range. In particular the scattering by plasmons is key to explain the anomalous low mobility of $100 \text{ cm}^2 \text{V}^{-1} \text{s}^{-1}$ above $n = 10^{19} \text{ cm}^{-3}$. Even through the inclusion of electron-plasmon scattering a residual discrepancy between theory and experiment is still observed, which we ascribe to the simplified models adopted in the description of electronic scattering with electron-hole pairs and impurities. This observation leads us to suggest that the origin of the mobility overestimation in earlier calculations could be connected with the neglect of electron-plasmon scattering^{54,55}.

¹ S. Lal, S. Link, and N. J. Halas, Nat. Photonics **1**, 641 (2007).

² R. J. Walters, R. V. A. van Loon, I. Brunets, J. Schmitz, and A. Polman, Nat. Mater. **9**, 21 (2010).

³ H. A. Atwater and A. Polman, Nat. Mater. **9**, 205 (2010).

⁴ M. L. Brongersma, N. J. Halas, and P. Nordlander, Nat. Nanotechnol. **10**, 25 (2015).

⁵ E. Y. Lukianova-Hleb, X. Ren, R. R. Sawant, X. Wu, V. P.

- Torchilin, and D. O. Lapotko, Nat. Med. **20**, 778 (2013).
- ⁶ Z. Zhang, J. Wang, and C. Chen, Adv. Mater. **25**, 3869 (2013).
 - ⁷ S. Maier, *Plasmonics: Fundamentals and Applications* (Springer, 2007).
 - ⁸ J. M. Pitarke, V. M. Silkin, E. V. Chulkov, and P. M. Echenique, Rep. Prog. Phys. **70**, 1 (2007).
 - ⁹ E. Ozbay, Science **311**, 189 (2006).
 - ¹⁰ D. Bohm and D. Pines, Phys. Rev. **92**, 609 (1953).
 - ¹¹ D. Pines and J. R. Schrieffer, Phys. Rev. **125**, 804 (1962).
 - ¹² P. Nozières and D. Pines, Phys. Rev. **113**, 1254 (1959).
 - ¹³ S. L. Adler, Phys. Rev. **126**, 413 (1962).
 - ¹⁴ N. Wiser, Phys. Rev. **129**, 62 (1963).
 - ¹⁵ D. Pines, *Elementary Excitations in Solids* (Perseus, 1999).
 - ¹⁶ See Supplemental Material at [tobeaddedbypublisher](#), which includes Refs.^{45–63}.
 - ¹⁷ S. E. Aw, H. S. Tan, and C. K. Ong, J. Phys.: Condens. Matter **3**, 8213 (1991).
 - ¹⁸ M. Balkanski, A. Aziza, and E. Amzallag, Phys. Status Solidi B **31**, 323 (1969).
 - ¹⁹ M. Zacharias, C. E. Patrick, and F. Giustino, Phys. Rev. Lett. **115**, 177401 (2015).
 - ²⁰ P. Nozieres and D. Pines, Il Nuovo Cimento (1955-1965) **9**, 470 (1958).
 - ²¹ G. Mahan, *Many-Particle Physics* (Springer, 2000).
 - ²² S. Engelsberg and J. R. Schrieffer, Phys. Rev. **131**, 993 (1963).
 - ²³ H. Fröhlich, Advances in Physics **3**, 325 (1954).
 - ²⁴ C. Verdi and F. Giustino, Phys. Rev. Lett. **115**, 176401 (2015).
 - ²⁵ R. Jalabert and S. Das Sarma, Phys. Rev. B **41**, 3651 (1990).
 - ²⁶ M. Bernardi, D. Vigil-Fowler, J. Lischner, J. B. Neaton, and S. G. Louie, Phys. Rev. Lett. **112**, 257402 (2014).
 - ²⁷ F. E. Doany and D. Grischkowsky, Appl. Phys. Lett. **52** (1988).
 - ²⁸ A. Marini, Phys. Rev. Lett. **101**, 106405 (2008).
 - ²⁹ F. Giustino, S. G. Louie, and M. L. Cohen, Phys. Rev. Lett. **105**, 265501 (2010).
 - ³⁰ E. Cannuccia and A. Marini, Phys. Rev. Lett. **107**, 255501 (2011).
 - ³¹ S. Botti and M. A. L. Marques, Phys. Rev. Lett. **110**, 226404 (2013).
 - ³² B. Monserrat, N. D. Drummond, C. J. Pickard, and R. J. Needs, Phys. Rev. Lett. **112**, 055504 (2014).
 - ³³ G. Antonius, S. Poncé, P. Boulanger, M. Côté, and X. Gonze, Phys. Rev. Lett. **112**, 215501 (2014).
 - ³⁴ Y. Liang and L. Yang, Phys. Rev. Lett. **114**, 063001 (2015).
 - ³⁵ A. Damascelli, Z. Hussain, and Z.-X. Shen, Rev. Mod. Phys. **75**, 473 (2003).
 - ³⁶ S. Moser, L. Moreschini, J. Jaćimović, O. S. Barišić, H. Berger, A. Magrez, Y. J. Chang, K. S. Kim, A. Bostwick, E. Rotenberg, L. Forró, and M. Grioni, Phys. Rev. Lett. **110**, 196403 (2013).
 - ³⁷ F. Caruso, H. Lambert, and F. Giustino, Phys. Rev. Lett. **114**, 146404 (2015).
 - ³⁸ F. Caruso and F. Giustino, Phys. Rev. B **92**, 045123 (2015).
 - ³⁹ E. Bustarret, C. Marcenat, P. Achatz, J. Kacmarcik, F. Levy, A. Huxley, L. Ortega, E. Bourgeois, X. Blase, D. Debarre, and J. Boulmer, Nature **444**, 465 (2006).
 - ⁴⁰ E. A. Ekimov, V. A. Sidorov, E. D. Bauer, N. N. Mel'nik, N. J. Curro, J. D. Thompson, and S. M. Stishov, Nature **428**, 542 (2004).
 - ⁴¹ L. Boeri, J. Kortus, and O. K. Andersen, Phys. Rev. Lett. **93**, 237002 (2004).
 - ⁴² K.-W. Lee and W. E. Pickett, Phys. Rev. Lett. **93**, 237003 (2004).
 - ⁴³ X. Blase, C. Adessi, and D. Connétable, Phys. Rev. Lett. **93**, 237004 (2004).
 - ⁴⁴ F. Giustino, M. L. Cohen, and S. G. Louie, Phys. Rev. B **76**, 165108 (2007).
 - ⁴⁵ L. Hedin, Phys. Rev. **139**, A796 (1965).
 - ⁴⁶ W. G. Aulbur, L. Jönsson, and J. W. Wilkins, Solid State Phys. **54**, 1 (2000).
 - ⁴⁷ M. S. Hybertsen and S. G. Louie, Phys. Rev. B **34**, 5390 (1986).
 - ⁴⁸ S. Engelsberg and P. M. Platzman, Phys. Rev. **148**, 103 (1966).
 - ⁴⁹ B. Lundqvist, Phys. Kondens. Mater. **6**, 193 (1967).
 - ⁵⁰ D. C. Langreth, Phys. Rev. B **1**, 471 (1970).
 - ⁵¹ A. W. Overhauser, Phys. Rev. B **3**, 1888 (1971).
 - ⁵² F. Mousty, P. Ostojá, and L. Passari, J. Appl. Phys. **45** (1974).
 - ⁵³ S. Das Sarma and F. Stern, Phys. Rev. B **32**, 8442 (1985).
 - ⁵⁴ J. R. Meyer and F. J. Bartoli, Phys. Rev. B **36**, 5989 (1987).
 - ⁵⁵ O. D. Restrepo, K. Varga, and S. T. Pantelides, Appl. Phys. Lett. **94**, 212103 (2009).
 - ⁵⁶ P. Hohenberg and W. Kohn, Phys. Rev. **136**, B864 (1964).
 - ⁵⁷ W. Kohn and L. J. Sham, Phys. Rev. **140**, A1133 (1965).
 - ⁵⁸ P. Giannozzi *et al.*, J. Phys.: Condens. Matter **21**, 395502 (2009).
 - ⁵⁹ N. Troullier and J. L. Martins, Phys. Rev. B **43**, 1993 (1991).
 - ⁶⁰ A. Marini, C. Hogan, M. Gruning, and D. Varsano, Comp. Phys. Commun. **180**, 1392 (2009).
 - ⁶¹ J. Noffsinger, F. Giustino, B. D. Malone, C.-H. Park, S. G. Louie, and M. L. Cohen, Comp. Phys. Commun. **181**, 2140 (2010).
 - ⁶² S. Baroni, S. de Gironcoli, A. Dal Corso, and P. Giannozzi, Rev. Mod. Phys. **73**, 515 (2001).
 - ⁶³ A. A. Mostofi, J. R. Yates, Y.-S. Lee, I. Souza, D. Vanderbilt, and N. Marzari, Comp. Phys. Commun. **178**, 685 (2008).